Available online at www.sciencedirect.com
SCIENCE DIRECT®
ELSEVIER
Earth and Planetary Science Letters xx (2006) xxx–xxx
EPSL
www.elsevier.com/locate/epsl

Oscillating and stagnating plumes in the Earth's lower mantle

Henri Samuel *, David Bercovici

Department of Geology and Geophysics, Yale University, USA

Received 7 November 2005; received in revised form 21 March 2006; accepted 21 April 2006

Editor: V. Courtillot

Abstract

We investigate the coupled effects of mineralogy and pressure on the dynamics of axisymmetric thermochemical plumes in the lower mantle, using both high resolution numerical experiments and simple analytical theory. We focus on the effect of composition on the compressibility which has not been studied before. Our results show that the effect of mineralogy is considerable: For relatively low Si enrichment, the compressibility of the plume and of the surrounding mantle is similar therefore the compositional density excess of the plume is constant with depth. This leads to an oscillatory behavior in plume head vertical position with time, similar to previous work [A. Davaille. Simultaneous generation of hotspots and superswells by convection in a heterogeneous planetary mantle. Nature, 402 (1999) 756–760.]. Si-enriched compositions instead induce a lower compressibility for the thermochemical plume with respect to the surrounding mantle, implying an increase of the compositional density excess with decreasing depth. Therefore, although thermochemical plumes can fully develop and rise toward the surface, their ascent may be impeded by the chemical density excess, leading to the stagnation of large plume heads at various depths in the lower mantle. As a consequence, Si-enriched thermochemical plumes may display broad (~1200 km wide) negative seismic velocity anomalies at various lower mantle depths, which may not necessarily be associated with upwelling currents. In addition, the coupling between mineralogy and dynamics may provide an efficient mechanism for the long term survival of compositional heterogeneity in the lower mantle.

Keywords: thermochemical plumes; convection; compositional heterogeneity; lower mantle; oscillatory

1. Introduction

Both geochemical and seismological observations suggest that the Earth's mantle is heterogeneous in major element composition. Mass balance calculations based either on carbonaceous chondrites [2] or enstatite chondrites [3] suggest that a significant part of the mantle is enriched in Si and Fe, relative to a pyrolitic composition [4] which is representative of the 'shallow' mantle that produces oceanic crust and residual lithosphere at mid-oceanic ridges. Moreover, seismological observations combined with geodynamical considerations [5] suggest that the lowermost mantle has a chemically distinct composition with respect to a pyrolitic mantle.

Several mechanisms can be advanced to explain mantle heterogeneity in major elements: (i) The recycling and segregation of the oceanic crust in the lower mantle [6,7] which would imply the presence of Si and Fe enriched material in the lowermost mantle, (ii) core–

* Corresponding author. Now at Geophysical Fluid Dynamics, Institut für Geophysik, ETH Hönggerberg, Zürich, Switzerland.
E-mail addresses: henri.samuel@erdw.ethz.ch (H. Samuel), david.bercovici@yale.edu (D. Bercovici).

0012-821X/$ - see front matter © 2006 Elsevier B.V. All rights reserved.
doi:10.1016/j.epsl.2006.04.037

mantle chemical interactions [8] which would enrich the mantle in iron relative to a pyrolitic composition, (iii) the freezing of an early magma ocean which would lead to the presence of Si-enriched material [9,10] as a result of fractional crystallization.

The Earth's mantle is therefore likely to be heterogeneous in terms of its major element composition, and more specifically, that some part of the deep mantle is enriched in Si and Fe relative to a pyrolitic composition. As suggested by previous studies [11], this enrichment would produce a positive compositional density contrast (i.e., the presence of intrinsically denser material) with respect to the surrounding mantle. Since density differences are the driving forces of convection, even small compositional density contrast may have an important effect on the dynamics of the Earth's mantle, especially if they are of the same order as thermal density contrasts ($\sim -2\%$ in the lower mantle) but of opposite sign.

Previous studies have shown that indeed the presence of even small (e.g., 1%) compositional density contrasts significantly affect mantle dynamics at various scales. On the global scale, the presence of compositional density contrasts may: (1) produce a great variety of convective patterns [12], including the formation of large scale oscillating domes, possibly responsible of the presence of superswells [1]; (2) affect the stirring processes by producing isolated regions with distinct stirring efficiencies [13], thus providing a possible mechanism to explain the systematic differences in isotopic compositions observed for mid ocean ridge basalts and Ocean Island Basalts (OIB) [14]; (3) enhance the stability and the longevity of mantle plumes [15]. On regional scales, the influence of compositional density contrasts has also a first order impact on the dynamics and on the interpretation of surface observations. Farnetani and Samuel [16] have shown that the presence of compositional density contrasts provide a geodynamically consistent framework to interpret (i) the extreme variability observed for OIB isotopic compositions as well as their longevity in the south central Pacific region; (ii) the irregular and broad seismic velocity anomalies revealed by seismic tomography in the lowermost mantle (e.g., [17]). Furthermore, in a recent study, Lin and van Keken [18] show that the presence of compositional density contrasts explains the multiple and irregular pulses of major volcanic eruptions for large igneous provinces, revealed by geochronological data, which are difficult to produce by a purely thermal origin.

While these studies all underline the importance of compositional heterogeneities on mantle dynamics at various scales and for the interpretation of surface observations, they all assume that the compositional density contrast is constant and the influence of composition and pressure is not taken into account. Therefore, this paper focuses on these features of variable compositional density contrasts by considering the dynamics of axisymmetric thermochemical plumes in the lower mantle. We first show, on the basis of mineral physics, that the compositional density contrast between a chemically distinct material and a pyrolitic reference mantle can significantly vary with pressure, depending on the composition considered. We then investigate the effect of composition- and pressure-dependence of the compositional density contrast on the stability of a thermochemical plume surrounded by a pyrolitic mantle, using both numerical and semi-analytical models. The effects are shown to have a significant impact on the fate of plumes and plume heads in the Earth's mantle.

2. Pressure dependence of the compositional density contrast

For the purpose of this study we consider the system SiO_2–FeO–MgO and focus on lower mantle phases (Mg,Fe)SiO_3 perovskite and (Mg,Fe)O magnesiowüstite. In this framework, any given composition can be defined by three ratios. The first two are the silica and the iron molar ratios: $x\mathrm{Si}=n\mathrm{Si}/(n\mathrm{Fe}+n\mathrm{Mg})$ and $x\mathrm{Fe}=n\mathrm{Fe}/(n\mathrm{Fe}+n\mathrm{Mg})$, where nSi, nFe and nMg represent the number of moles of Si, Fe and Mg, respectively. Note that $n\mathrm{Fe}+n\mathrm{Mg}$ is equal to the total number of moles of (Mg,Fe)SiO_3 perovskite and (Mg,Fe)O magnesiowüstite. Thus xSi expresses the molar proportion of perovskite and $1-x\mathrm{Si}$ is the complementary molar proportion of magnesiowüstite. The third ratio is the iron–magnesium partition coefficient between magnesiowüstite and perovskite: $K\mathrm{Fe}=\frac{x\mathrm{Fe}^{\mathrm{mw}}(1-x\mathrm{Fe}^{\mathrm{pv}})}{x\mathrm{Fe}^{\mathrm{pv}}(1-x\mathrm{Fe}^{\mathrm{mw}})}$, which we assume to be constant and equal to 3.5, as suggested by [19].

For a given material, the variation of its density ρ at a given temperature T with lithostatic pressure P is controlled by the value of its bulk modulus $K_T=\rho(\partial P/\partial\rho)_T$. As shown in Table 1 perovskite and magnesiowüstite have very different bulk modulii, indicating that

Table 1
Thermodynamical parameters for perovskite and magnesiowüstite at ambient temperature

Parameters	$\mathrm{Mg}_{x_{\mathrm{Mg}}}^{\mathrm{pv}}\ \mathrm{Fe}_{x_{\mathrm{Fe}}}^{\mathrm{pv}}\mathrm{SiO}_3$	$\mathrm{Mg}_{x_{\mathrm{Mg}}}^{\mathrm{mw}}\ \mathrm{Fe}_{x_{\mathrm{Fe}}}^{\mathrm{mw}}\mathrm{O}$
K_T (GPa)	258	$161+7.5x_{\mathrm{Fe}}^{\mathrm{mw}}$
K'	4.1	4.1
ρ (kg m^{-3})	$4108+1070x_{\mathrm{Fe}}^{\mathrm{pv}}$	$3583+2280x_{\mathrm{Fe}}^{\mathrm{mw}}$

Values of K_T and $K'=\partial K_T/\partial P$ are from [31]. The iron dependence of ρ and K_T are taken from [32]. The superscripts pv and mw stand for (Mg,Fe)SiO_3 perovskite and (Mg,Fe)O magnesiowüstite, respectively.

magnesiowüstite is more compressible than perovskite. Consider a material whose composition in major elements differs from a reference pyrolitic mantle (i.e., $x\mathrm{Si}_{\mathrm{py}}=0.68$ and $x\mathrm{Fe}_{\mathrm{py}}=0.11$). Using mineral physics considerations (following the approach described in Appendix A) and mineral physics data listed in Table 1, one can calculate the density at ambient temperature for a range of lower mantle pressures, for the reference pyrolitic mantle ρ_{py} as well as density for general compositions ρ_χ. One can thus deduce a profile of compositional density contrast between the two materials $\Delta\rho_\chi=\rho_\chi-\rho_{\mathrm{py}}$. Such profiles, normalized by ρ_{py} are represented in Fig. 1 for three different compositions. The ratio $\beta=\Delta\rho_\chi/\rho_{\mathrm{py}}$ may vary with pressure depending on the composition of the chemically distinct material with respect to the reference pyrolitic mantle chosen. Since reasonable iron enrichment/depletion (i.e., a change in xFe with respect to that for a pyrolitic $x\mathrm{Fe}=0.11$) does not affect the mineralogical composition (i.e., the molar proportions between perovskite and magnesiowüstite are not modified) the average bulk modulus of the whole assemblage does not differ too much from the bulk modulus of a pyrolitic composition (see Table 1). Consequently, β varies little with pressure in this case (see profile corresponding to composition 1 in Fig. 1). In contrast, a Si enrichment/depletion will modify the molar proportions between perovskite and magnesiowüstite, resulting in a different bulk modulus for the whole assemblage with respect to the pyrolitic composition.

Following a similar approach described in [20], we determine the approximate analytical expressions for β_0 and $\mathrm{d}\beta/\mathrm{d}z$ for a material with a given xSi and xFe for the ranges xFe [0.09–0.20] and xSi [0.5–1]. We find a simple approximate analytical expression for the dependence of β_0 with xSi and xFe: $\beta_0=33.0027\ 10^{-2}(x\mathrm{Fe}-x\mathrm{Fe}_{\mathrm{py}})[1-0.7126(x\mathrm{Si}-x\mathrm{Si}_{\mathrm{py}})]$. We obtain an even simpler expression of $\mathrm{d}\beta/\mathrm{d}z$ (given in km^{-1}): $\mathrm{d}\beta/\mathrm{d}z=17.2377\ 10^{-6}(x\mathrm{Si}-x\mathrm{Si}_{\mathrm{py}})[1-0.6474(x\mathrm{Si}-x\mathrm{Si}_{\mathrm{py}})]$.

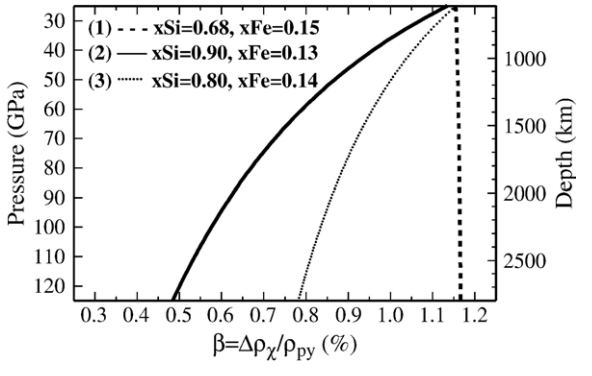

Fig. 1. Pressure dependence of the compositional density contrast with respect to a pyrolitic reference composition ($x\mathrm{Si}_{\mathrm{py}}=0.68$ and $x\mathrm{Fe}_{\mathrm{py}}=0.11$) at ambient temperature for three distinct compositions. The equivalent mantle depth is represented on the left vertical axis.

The ratio β can vary by 100% for composition 2 (see Fig. 1) and up to 200% for even more Si-enriched compositions (e.g., $x\mathrm{Si}=0.95$ and $x\mathrm{Fe}=0.13$). The sign of the variation $\mathrm{d}\beta/\mathrm{d}z$ is almost entirely related to the Si enrichment/depletion of the chemically distinct material with respect to the reference pyrolitic mantle while the magnitude of this variation depends on both the Fe and Si enrichment/depletion (e.g., see profiles corresponding to compositions 1 and 2 in Fig. 1).

Since the dynamics of convection can be strongly influenced by the presence of even very small compositional density contrasts (e.g., [1,11,12,14,15]), one should expect that an important variation of β with pressure, as shown in Fig. 1 for Si-enriched compositions, may have a first order impact on the dynamics of thermochemical plumes. Therefore, the fundamental question we address in this paper is how the pressure dependence of β will affect the convective stability of plumes? We first investigate the problem by the means of numerical modeling experiments, and we subsequently establish a semi-analytical model to study the physical processes that play a role on the dynamics of such thermochemical plumes.

3. Numerical experiments

In order to investigate the pressure and compositional dependence of the chemical density contrast $\Delta\rho_\chi/\rho_{\mathrm{py}}$ on the dynamics of thermochemical mantle plumes we set up numerical experiments using the convection code Stag3D [21] in 2D cartesian geometry.

3.1. Numerical model description

The code, described in detail in [21] solves for the conservation of mass, momentum and energy and the conservation of a compositional field χ in the limit of infinite Prandtl number. The compositional field allows us to model the presence of compositional density contrasts $\Delta\rho_\chi$ which are small compared to the reference mantle density.

The characteristic scales used to normalize the governing equations are the mantle thickness $H=3000$ km, the mean lower mantle density $\rho_0=4500\ \mathrm{kg\ m}^{-3}$, the maximum temperature difference allowed between the thermochemical plume and the reference mantle $\Delta T=1000$ K, the reference mantle viscosity $\eta_0=6.08\ 10^{21}$ Pa s. The thermal diffusion timescale H^2/κ is used where $\kappa=10^{-6}\ \mathrm{m}^2\ \mathrm{s}^{-1}$ is the thermal diffusivity.

Two non-dimensional numbers appear from the normalization of the conservation equations. The first is the Rayleigh number,

$$Ra = \frac{\rho_0 \alpha \Delta T g H^3}{\eta_0 \kappa}, \quad (1)$$

where $g=10$ m^2 s^{-1} is the gravitational acceleration and $\alpha=2.5\ 10^5$ K^{-1} is the thermal expansion coefficient. The choice of parameters listed above leads to a value of $Ra=5\ 10^6$.

The second dimensionless number is the buoyancy number: the ratio between the stabilizing compositional density contrast $\Delta\rho_\chi$ material over the destabilizing thermal density contrast:

$$B = \frac{\Delta\rho_\chi}{\rho_0 \alpha \Delta T} = \frac{\beta}{\alpha \Delta T}. \quad (2)$$

Viscosity is temperature dependent, according the following relationship:

$$\eta = \eta_0 e^{-\theta \ln\gamma}, \quad (3)$$

where θ is the dimensionless potential temperature and γ is the maximum viscosity contrast allowed. Both B and γ are varied systematically.

Density ρ varies according to the linear equation of state:

$$\rho = \rho_0[1-\alpha(T-T_0) + \chi\beta], \quad (4)$$

where χ expresses the composition which ranges from 0 (purely pyrolitic mantle) to 1 (purely chemically distinct material), and β is the compositional dependence of the density and may be depth dependent according to Profile 2 of Fig. 1.

The top and bottom surfaces are impermeable and free slip while reflective boundary conditions are applied to the vertical surfaces. We performed calculations on a grid composed of 768 horizontal points and 512 vertical points with an aspect ratio of 1:5:1, yielding a spatial resolution of 5.8 km for both horizontal and vertical directions.

The evolution of the compositional field is solved using a Lagrangian formalism, with a marker chain technique [22]. Tracers are used to delineate the interface between the reference mantle and the compositionally distinct material, which is initially a rectangle of (dimensionless) length and height 1.5 and 0.1, respectively, located at the bottom of our model domain. At each time step the tracers are advected using a fourth order Runge–Kutta scheme and the tracers positions are fitted by cubic splines. Tracers are added or removed according to curvature and length criteria along the curve obtained by the spline fitting (i.e., by requiring that the product of the curvature times the length for two consecutive tracers along the curve is $\pi/2500$), thus preventing the use of unnecessary markers. This marker chain method has been benchmarked against another convection study [22] and for the purpose of our study was found to be more reliable and computationally less expensive than the use of full (space filling) tracer technique. Moreover, conservation of mass of the compositional anomaly is guaranteed by checking that the absolute value of the mass error [23]

$$\Delta M_{mass} = \frac{\int \chi \mathrm{d}V - \left(\int \chi \mathrm{d}V\right)^{\text{initial}}}{\left(\int \chi \mathrm{d}V\right)^{\text{initial}}} \quad (5)$$

(where V is the volume of the computational domain) is less than 0.2%.

At the initial time $t=0$, the dimensionless potential temperature θ is zero everywhere, except in a small area whose horizontal location corresponds to the vertical axis of symmetry $x=0$ while its vertical location corresponds to the interface between the chemically denser material and the reference mantle located at the dimensionless height $z=0.1$. During all the calculation, we impose in this area of dimensionless length and height 0.009 and 0.017, a heating patch with a potential temperature $\theta=1$. The location and the dimensions of the heating patch were chosen in order to generate the thermochemical plume at the interface between the dense material and the overlying mantle and to reduce the initial dimensions of the plume head.

3.2. Results

In order to investigate the influence of compositional and pressure (or depth) dependence of β on the dynamics of axisymmetric thermochemical plumes, we run two numerical experiments corresponding to the two extreme cases shown in the profiles 1 and 2 of Fig. 1. In terms of $\Delta\rho_\chi$, both compositions 1 and 2 can be defined by $\beta_0=\beta(z=0)$ and $\mathrm{d}\beta/\mathrm{d}z$. For simplicity, we do not consider the curvature observed in profiles of Fig. 1. For composition 1, $\beta_0=1.18\%$ and $\mathrm{d}\beta/\mathrm{d}z=0$ km^{-1} while for composition 2, $\beta_0=0.49\%$ and $\mathrm{d}\beta/\mathrm{d}z=3\ 10^{-6}$ km^{-1}.

3.2.1. Case where $d\beta/dz=0$

Fig. 2a–c show snapshots of the thermochemical plume for experiment 1, revealed by its compositional field χ corresponding to composition 1 (see Fig. 1). The thermochemical plume first rises to its maximum height of about 2000 km (Fig. 2a). At this height, the buoyancy loss by thermal diffusion makes the plume head stop and fall back towards its source (Fig. 2b). Note that the presence of a second, smaller plume head is due to the

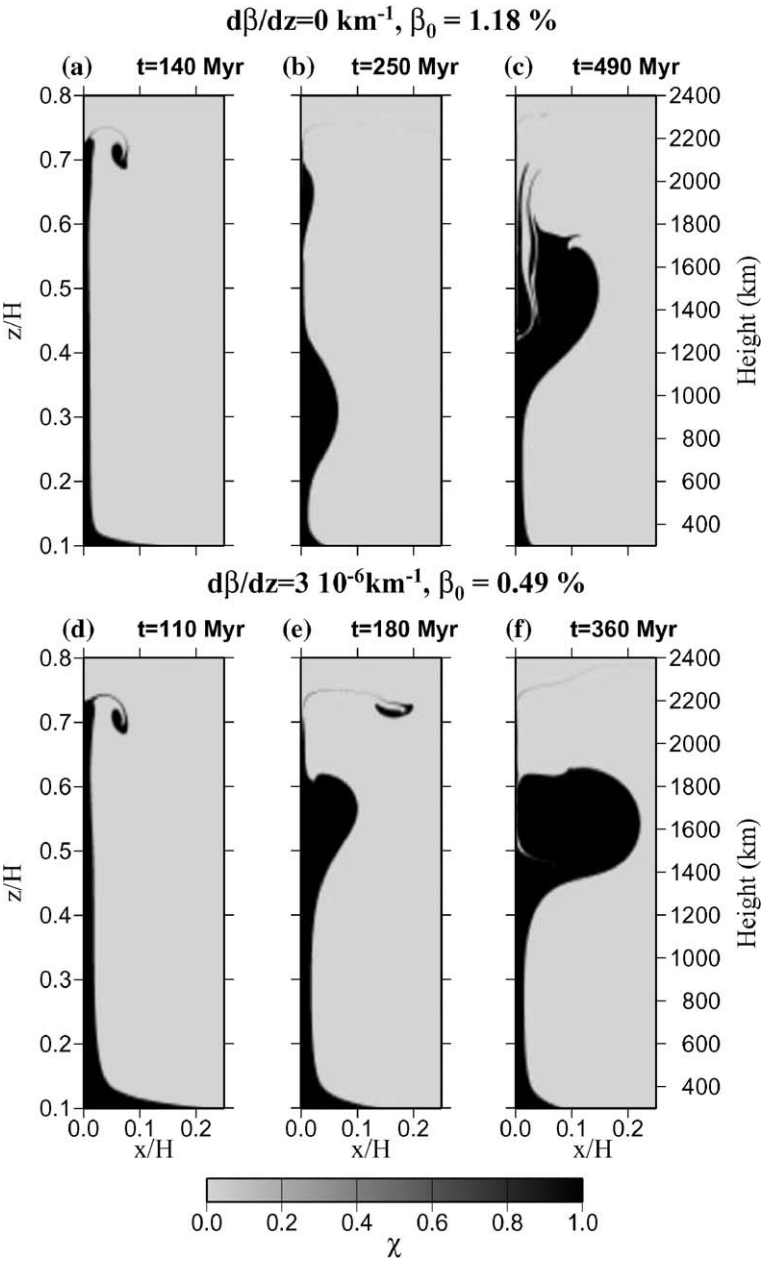

Fig. 2. Snapshots of thermochemical plume revealed by the compositional field χ for two distinct mineralogical compositions with respect to a pyrolitic reference. Top: case corresponding to composition 1 (xSi=0.68, xFe=0.15) at 140 Myr (a), 250 Myr (b) and 490 Myr (c). Bottom: case corresponding to composition 2 (xSi=0.90, xFe=0.13) at 110 Myr (d), 180 Myr (e) and 360 Myr (f).

generation of a purely thermal plume at the top of the thermochemical plume head, which entrains part of the dense material toward the surface by viscous coupling. During its descent, the plume head is continuously fed by hotter material injected through the conduit, and thus regains enough buoyancy to rise up again except only to a lower height of about 1400 km (Fig. 2c). The mean conduit half width is 45 km and the volumetric flux Q of chemically distinct material inside the plume conduit is fairly constant with depth and time at about 0.13 km^3 yr^{-1}. Indeed, once the steady flux Q is reached at the heat source, it remains constant, which is in good agreement with a previous study [24]. This causes the volume of the plume head to increase at a fairly constant rate. After reaching a critical volume, the plume head tends to split and portions of dense material fall back toward the source,

but to either side of the conduit, yielding another cycle of vertical oscillations of the plume head. The number of oscillations depends on the value of $\Delta\rho_\chi$ but in some cases (not presented here) we have observed up to 6 oscillations with a period of ~200 Myr. This oscillatory behavior of the plume head is also shown in Fig. 3a which displays the time evolution of z_{Rmax}, the vertical location of the maximum value of the plume head radius, which gives a good estimate of the vertical location of the plume head center.

Although our experiments concern thermochemical plumes rather than domes originated from a thick chemically denser layer, the physics is similar to what is observed in laboratory experiments [1]. Moreover, our numerical experiment shows that even when starting with a relatively small volume for the plume head and modest value for the conduit half width (~45 km), the presence of a small compositional density contrast leads, after some time, to relatively large thermochemical plume heads with a half width close to 500 km after few hundred Myr, without the need of a source region much bigger than D'' layer.

3.2.2. Case where $d\beta/dz \neq 0$

Fig. 2d–f show snapshots of the thermochemical plume for experiment 2, revealed by its compositional field χ corresponding to composition 2 (i.e., xFe=0.13 and xSi=0.9, see Fig. 1). For this experiment we found that the mean value of the conduit half width is again 45 km and Q=0.17 km^3 yr^{-1} which, similar to experiment 1, is also fairly constant in time and space. The initiation of the plume head is similar to the case where β is constant (i.e., composition 1). However, after reaching its maximum height of about 2200 km (Fig. 2d), the plume head falls back to approximately 1600 km (Fig. 2e) and then reaches a level of neutral buoyancy, z_{NB} that is roughly constant with time (Fig. 2f). As in the case where β is constant, parts of the plume head often detach and fall back to the source after a critical plume head volume has been reached. However, this does not affect significantly the vertical location of the level of neutral buoyancy. Thus in all cases, after the plume head reaches z_{NB}, its volume continues growing with time but the dense material roughly remains at $z \cong z_{\mathrm{NB}}$. The stagnant plume head regime observed in this case is also revealed in Fig. 3b which displays the time evolution of z_{Rmax}, the vertical location of the maximum radius of the plume head.

The results of the two numerical experiments displayed in Figs. 2 and 3 clearly show the strong mutual influence of the mineralogy- and pressure-dependence of β. In the case where β is constant (corresponding to an iron enrichment only of the dense material relative to a pyrolitic reference mantle), we observe an oscillatory behavior of the plume head. In contrast, a depth dependent β damps the oscillatory behavior and leads to a plume head that stagnates at a level of neutral buoyancy.

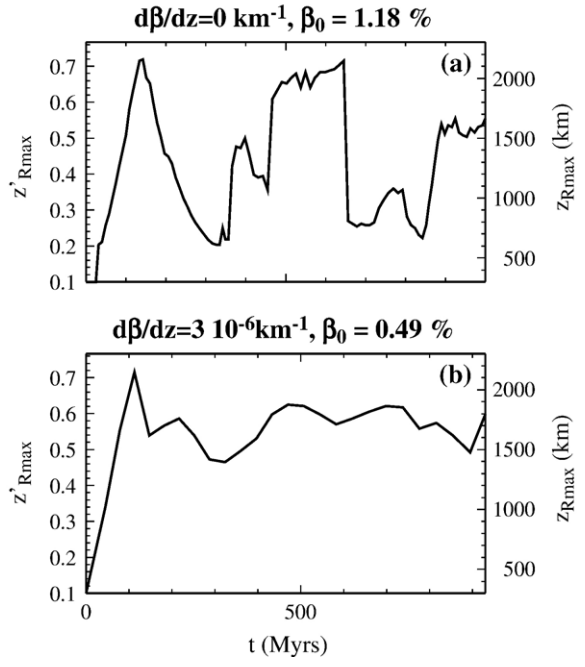

Fig. 3. Results from the numerical experiments 1 (a) and 2 (b). Time evolution of z_{Rmax}, the vertical location of the maximum plume head radius.

4. Diapir-conduit model

In order to elucidate the physical mechanisms observed in the numerical experiments described in the previous section, we set up a semi-analytical model, following the approach of [25,26]. We consider a diapir-conduit model in cylindrical coordinates (z,r) (Fig. 4) where the thermochemical plume is composed of a spherical head R_{h}, connected to the source by a thin cylindrical supply conduit of constant radius r_{c}, and thus of cross-sectional area $A=\pi r_{\mathrm{c}}^2$. Mass conservation for the spherical diapir requires:

$$\frac{\mathrm{d}R_{\mathrm{h}}}{\mathrm{d}t} = \frac{Q - AU_{\mathrm{h}}}{4\pi R_{\mathrm{h}}^2}, \tag{6}$$

where t is time, Q is the constant volumetric influx of hot but chemically denser material, and U_{h} is the Stokes velocity for the plume head. Assuming a small plume viscosity $\eta=\eta_0/\gamma^*$ (where γ^* is the viscosity contrast) with respect to the surrounding colder mantle viscosity η_0 [27], we find that

$$U_{\mathrm{h}} = \frac{\Delta\rho g R_{\mathrm{h}}^2}{3\eta_0}. \tag{7}$$

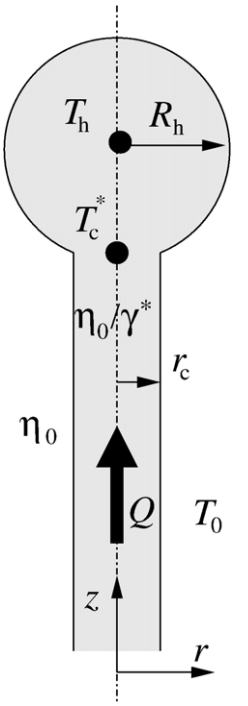

Fig. 4. Schematic representation of the semi-analytical plume feeding model. See text for further definition of the symbols.

Note that to facilitate the comparison between the numerical experiments and the diapir-conduit model, we show in Appendix B that γ^* and γ, the maximum viscosity contrast allowed for the numerical experiments (which enters into Eq. (3)) are related according to: $\gamma^*=\gamma/1.95$. Contrary to [25], both thermal and compositional effects are taken into account in the buoyancy of the plume $\Delta\rho g$. The effective density difference between the plume and the surrounding mantle follows the linear equation of state (4) with $\chi=1$; thus $\Delta\rho=\rho_0[\alpha(T_h(z)-T_0)-\beta(z)]$, where T_0 and ρ_0 are the reference temperature and density and T_h is the mean temperature of the plume head.

Conservation of energy requires that

$$\frac{d}{dt}\left(\frac{4\pi}{3}R_h^3\rho_0 C_P T_h\right)=q_h+(Q-AU_h)\rho_0 C_P T_c^*, \qquad (8)$$

where T_c^* is the horizontally averaged temperature at the top of the conduit, just below the plume head, $q_h=-2\pi R_h k(T_h-T_0)$ is the conductive heat loss by the spherical head whose estimation can be found in Appendix C.1; $k=\kappa\rho_0 C_P$ is the thermal conductivity and C_P is the specific heat. The second term on the right hand side of Eq. (8) accounts for the heat provided by the feeding conduit. Making the Boussinesq approximation that $\rho\cong\rho_0$ and C_P is constant and using Eq. (6), Eq. (8) can be recast as

$$\frac{dT_h}{dt}=\frac{3}{R_h^2}\left[-\kappa\frac{(T_h-T_0)}{2}+\frac{(Q-AU_h)(T_c^*-T_h)}{4\pi R_h}\right]. \qquad (9)$$

An additional relationship is required in order to evaluate the temperature at the top of the conduit T_c^*. The latter is obtained by considering the steady heat loss from the sides of the conduit, which is:

$$\frac{d(U_c A\rho_0 C_P T_c)}{dz}=q_c=-\pi r_c\frac{k(T_c-T_0)}{r_c}, \qquad (10)$$

where T_c is the horizontally averaged conduit temperature at any height z, and U_c is the mean vertical velocity inside the conduit. The estimation of q_c can be found in Appendix C.2. Making the reasonable assumption (see results of Section 3) that the volumetric flux in the conduit is constant, then $U_c A=Q$ is constant and Eq. (10) becomes:

$$\frac{dT_c}{dz}=-\frac{\pi\kappa(T_c-T_0)}{Q}, \qquad (11)$$

the solution of which, when evaluated at the plume head height z_h, gives T_c^{4*}. Finally the relationship between the plume head height z_h and its velocity is:

$$\frac{dz_h}{dt} = U_h. \tag{12}$$

Eqs. (6), (7), (9), (11), (12) are non-dimensionalized using the following characteristic scales: $\sqrt{A/(4\pi)}$ for distance, $\sqrt{A^3/4\pi Q^2}$ for time and $\Delta T = T(z_0) - T_0$ for temperature where z_0 is the vertical location of the plume source. This yields the following system of equations:

$$\frac{dR_h'}{dt'} = \frac{1}{R_h'^2}(1 - U_h') \tag{13}$$

$$U_h' = B_T(\theta_h' - B)R_h'^2 \tag{14}$$

$$\frac{d\theta_h'}{dt'} = -\frac{6\theta_h'}{PeR_h'^2} + \frac{3}{R_h'^3}(1 - U_h')(\theta_c^{*\prime} - \theta_h') \tag{15}$$

$$\frac{dz_h'}{dt'} = U_h' \tag{16}$$

$$\frac{d\theta_c'}{dz'} = -\frac{\theta_c'}{Pe}, \tag{17}$$

where the primes denote dimensionless values, $\theta_h' = (T_h - T_0)/\Delta T$ and $\theta_c' = (T_c - T_0)/\Delta T$ and $\theta_c^{*\prime} = \theta_c'(z_h' - R_h')$. The buoyancy number B, defined in Eq. (2), is potentially a function of z according to the profiles of Fig. 1; to first order it is given by

$$B = B_0 + \left(\frac{1}{\alpha\Delta T}\frac{d\beta}{dz'}\right)z', \tag{18}$$

where $B_0 = \beta_0/(\alpha\Delta T)$ and $d\beta/dz' = L(d\beta/dz)$.

The dimensionless number,

$$B_T = \frac{A^2\rho_0\alpha\Delta T g}{12\pi\eta_0 Q} \tag{19}$$

is the ratio of the thermal buoyancy forces over viscous forces.

The third non-dimensional number is an effective Peclet number:

$$Pe = \frac{2Q}{\kappa\sqrt{A\pi}}. \tag{20}$$

While the solution of Eq. (17) is just $\theta_c' = e^{(z_0' - z')/Pe}$, Eqs. (13), (15) and (16) are integrated numerically using a fourth order Runge–Kutta algorithm, with the following set of initial conditions: $R_h' = R_0'$, $\theta_h' = \theta_c' = 1$, $z_h' = z_0' + R_0'$.

The initial value of the plume head radius R_0 is estimated following the relationship between γ, the viscosity ratio between the plume and the surrounding mantle, and δ the thickness of the source region $R_0 = \delta\gamma^{2/9}$ as given by [28]. The value of the influx Q is estimated by considering an empirically modified law for a laminar parabolic, buoyantly driven Poiseuille flow [27] inside the plume conduit of radius r_c near the source:

$$Q = c\frac{A^2\Delta\rho_0 g\gamma*}{8\pi\eta_0}, \tag{21}$$

where $\Delta\rho_0 = \rho_0(\alpha\Delta T - \beta_0)$. The empirical constant $c = 1/2$ was chosen in order to give a good fit to the estimated values of Q from the numerical experiments. The use of Eq. (21) should not be interpreted as an implicit assumption of a Poiseuille-like flow inside the plume conduit, whatever the value of the empirical constant c could be. Here Eq. (21) is only used to specify a value of Q provided at the source which, by standard scaling analysis, should depend on parameters such as A, η_0 or $\Delta\rho_0$. The assumption of buoyantly driven Poiseuille flow inside the plume conduit together with a constant flux Q would imply: (1) a hydrostatic flow outside the conduit, (2) a widening of the plume conduit as the buoyancy inside the conduit decreases (as a result of thermal diffusion). However, from the numerical experiments presented and from previous work [24] the presence of the thermochemical plume induces a non-hydrostatic pressure field outside the plume due to the return flow. This background flow appears to impinge on the plume conduit in such way as to keep the conduit radius fairly constant while the flux Q inside the conduit also remains nearly constant.

Eq. (21) and $R_0 = \delta\gamma^{2/9}$ are then used to determine the values of the initial plume head radius and the volumetric influx, respectively. A value of r_c (or A) needs also to be specified to estimate B_T and Pe; for this we chose the mean value of 45 km found for each numerical experiments 1 and 2.

4.1. Results

In order to compare the semi-analytical model described above with the numerical experiments presented in Section 3, we run two cases corresponding to each of the two numerical experiments 1 and 2 (named hereafter NE1 and NE2) with similar input parameters B_T, B and Pe. Table 2 summarizes the value

Table 2
Dimensionless numbers and parameters for the numerical experiments (NE) 1 and 2 and the corresponding semi-analytical (SA) runs

Parameters	NE1	SA1	NE2	SA2
B	0.47	0.47	0.20	0.20
B_T ($\times 10^{-3}$)	48	49	36	33
Pe	29	29	39	42
γ^*	51*	52	51*	50
$(1/L)\mathrm{d}\beta/\mathrm{d}z'$ ($\times 10^{-6}$ km^{-1})	0	0	3.0	3.0
Lr'_c (km)	45	45	45	45

The characteristic length scale L is 3000 km for NE and 22.5 km for SA.
*indicates values that have been calculated using $\gamma^* = \gamma/1.95$ (see text).

of these parameters for both NE1 and NE2 and the corresponding semi-analytical runs, named hereafter SA1 and SA2. Fig. 5a–c and e–f show the results for SA1 and SA2 runs, respectively.

4.1.1. Case where $d\beta/dz = 0$

The time evolution of the plume head height displayed in Fig. 5a shows that the oscillatory behavior observed for NE1 is well reproduced by SA1. The plume head first rises to a maximum height of ~2200 km. Fig. 5b shows the time evolution of $T_h - T_0$ and $T_c^* - T_0$ for SA1. During its ascent, the plume head loses heat by diffusion, consequently, its temperature T_h decreases. A comparable behavior is observed for T_c^*, the conduit temperature just below the plume head, and is even more pronounced since the conduit radius r_c is smaller than the plume head radius R_h. When the plume head reaches its maximum height, the heat lost during it ascent makes it denser than the surrounding mantle, and the plume head falls back down. During its descent, T_c^* increases rapidly because the conduit height decreases, leading to an increase of T_h (Fig. 5b). As a result of the T_h increase, the plume head becomes buoyant enough to rise up again (Fig. 5a) but to a smaller height of about ~1400 km. Fig. 5c shows the time evolution of the plume head radius R_h which scales as $t^{1/3}$, indicating that the volume of the plume head increases with time at a fairly constant rate. As required by mass conservation (13), the rate of increase of the plume head volume converges with time towards the value of the imposed influx Q as U_h converges towards 0. This increase of the plume head volume at a fairly constant rate with time decreases the effect of heat impact for the conduit: In fact when R_h increases, there is an imbalance between the plume head heat loss (i.e., the first term on the right hand side of Eq. (15)) which goes as R_h^{-2} and the dilution of plume head heat content by the increase of plume head volume (i.e., the second term on the right hand side of Eq. (15)) which goes as R_h^{-3}. Consequently, the plume head falls back again to the source and the cycle of ascent and descent is repeated. The amplitude of the oscillations decreases significantly with time because the volume of the plume head keeps increasing with time. The differences in the amplitude of the oscillations through time between NE1 and SA1 (compare Figs. 5a and 3a) is due, as mentioned earlier to the splitting of the plume head observed for NE1, which is not considered by the diapir-conduit model. However, we tested this conjecture by incorporating an arbitrary separation of the plume head in various cases for the diapir-conduit model, and indeed the damping of the oscillations of the plume head's position is removed.

4.1.2. Case where $d\beta/dz \neq 0$

The time evolution of the plume head height for SA2 displayed in Fig. 5d compares well with the results of NE2 (e.g., Fig. 3b). The plume head first reaches a maximum height of ~2400 km after ~100 Myr. Then, it falls back to a height of ~1500 km and remains at this level of neutral buoyancy for several hundred of Myr while its volume keeps increasing with time. Similar to SA1, the time evolution of the plume head radius displayed in Fig. 5f shows that R_h scales as $t^{1/3}$ because U_h converges rapidly towards 0 (see Fig. 5d). As a consequence, the rate of increase of the plume head volume converges rapidly to the value of the imposed influx Q, according to mass conservation requirements.

Fig. 5e shows the time evolution of $T_h - T_0$ and $T_c^* - T_0$ for SA2. The level of neutral buoyancy reached by the plume head corresponds to a height where an equilibrium between the heat lost by the plume head and the heat brought by the feeding conduit is reached, as shown in Fig. 5e. This 'steady' state is due to the fact that T_h is almost constant with time while T_c increases just enough to compensate the heat loss by the head.

For the specific case presented here the height of neutral buoyancy z_{NB} is located in the mid-mantle; however z_{NB} is controlled by the value of Pe, β_0 (or B) and $\mathrm{d}\beta/\mathrm{d}z$. A full analytical expression of z_{NB} can be obtained by noticing that:

$$U'_h = \frac{\mathrm{d}\theta'_h}{\mathrm{d}t'} = 0 \quad \text{at } z'_h = z'_{NB}. \tag{22}$$

Therefore, in that case, a non-trivial solution of Eq. (14) is $\theta'_h = B(z' = z'_{NB}) = B_{z_{NB}}$, as suggested by Fig. 5e. Then, under these assumptions, Eq. (15) yields

$$B_{z_{NB}}\left(1 + \frac{2R'_h}{Pe}\right) = \theta_c^{*\prime}. \tag{23}$$

Then, using Eq. (18), Eq. (23) can be recast as:

$$\left(B_0+\frac{1}{\alpha\Delta T}\frac{\mathrm{d}\beta}{\mathrm{d}z'}z'_{NB}\right)\left(1+\frac{2R'_h}{Pe}\right)=\theta^{*\prime}_{\mathrm{c}}. \tag{24}$$

The above equation is consistent with the assumptions made in Eq. (22) and with our diapir-conduit model for various values of $R'_{\mathrm{h}}\leq z'_{\mathrm{NB}}-z'_0$. This is due to the fact that while the vertical location of the plume head remains at $z'=z'_{\mathrm{NB}}$, the radius of the plume head keeps increasing with time because it is constantly fed by the conduit. Therefore, to obtain a solution z'_{NB} of Eq. (24), we chose the limiting case when the plume head's bottom reaches the source, that is for $R'_{\mathrm{h}}=z'_{\mathrm{NB}}-z'_0$. According to the solution of Eq. (17) (i.e., $\theta'_{\mathrm{c}}=e^{(z'_0-z')/Pe}$) this limiting case chosen implies that $\theta^{*\prime}_{\mathrm{c}}=1$. Thus, Eq. (24) becomes a second order polynomial equation

$$p_0=p_1z'_{\mathrm{NB}}+p_2z'^{\,2}_{\mathrm{NB}}=0, \tag{25}$$

with the coefficients of the polynomial:

$$\{p_0,p_1,p_2\}=\left\{B_0\left(1-\frac{2z'_0}{Pe}\right)-1,\ \frac{\mathrm{d}\beta}{\mathrm{d}z'},\ \frac{\mathrm{d}\beta}{\mathrm{d}z'}\left(\frac{2}{\alpha\Delta TPe}\right)\right\} \tag{26}$$

Since all the parameters entering in p_0, p_1 and p_2 are assumed to be positive, it follows from Eq. (26) that $p_2>0$. Moreover B_0 is assumed to be lower than 1 which implies that $p_0\leq 0$. Consequently, $p_0p_2\leq 0$ and then the discriminant $p_1^2-4p_0p_2$ is always strictly positive. Therefore Eq. (25) admits two real solutions

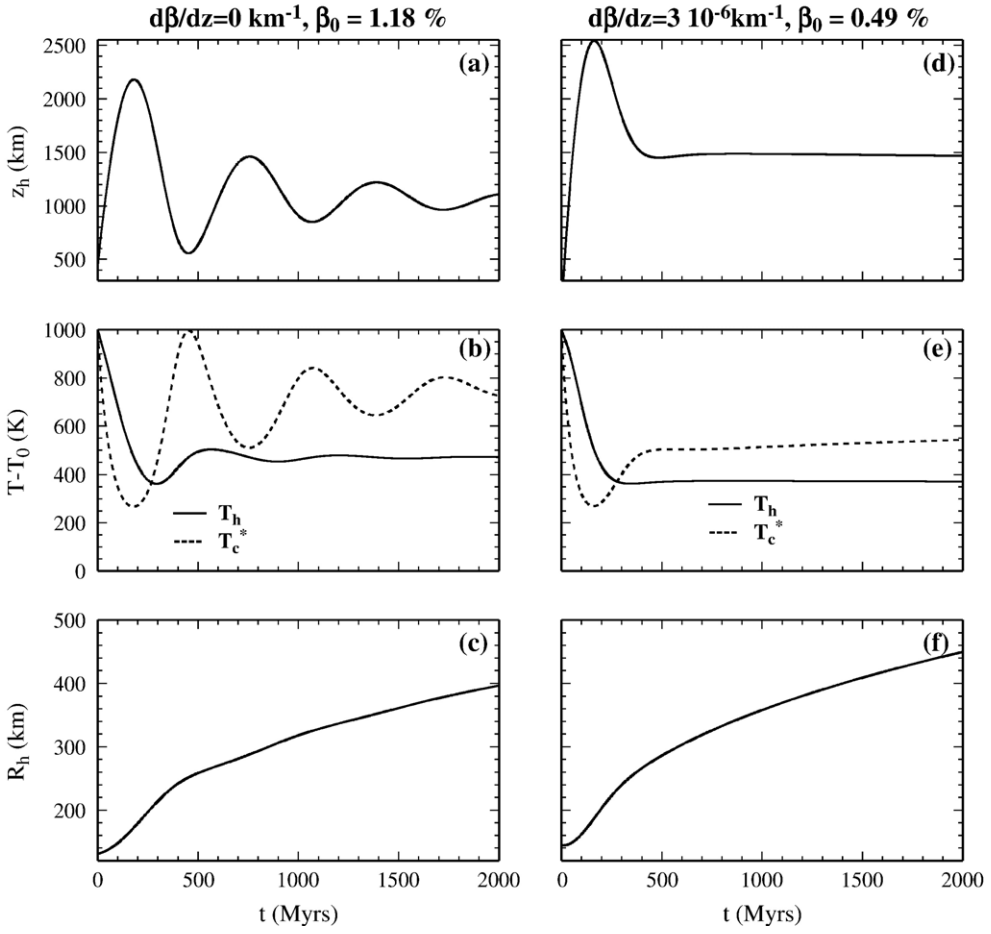

Fig. 5. Results of the diapir-conduit model. Left: case corresponding to a constant compositional density contrast (i.e., composition 1, see Fig. 1). (a) Time evolution of the center of the plume head height. (b) Time evolution of the temperature contrast with respect to the background temperature T_0 inside the plume head (plain line) and inside the conduit just below the plume head (dashed line). (c) Time evolution of the plume head radius R_{h}. Right: case corresponding to a depth/pressure compositional density contrast (i.e., composition 2, see Fig. 1). Frames (d)–(f) are equivalent to (a)–(f).

$z'^{-}_{\mathrm{NB}} = (-p_1 - \sqrt{p_1^2 - 4p_0p_2})/(2p_2)$ and $z'^{+}_{\mathrm{NB}} = (-p_1 + \sqrt{p_1^2 - 4p_0p_2})/(2p_2)$. However, for the range of Pe, B_0, $\mathrm{d}\beta/\mathrm{d}z'$ values, considered, z'^{-}_{NB} is always negative while z'^{+}_{NB} is always positive. We then only retain z'^{+}_{NB} as the physically meaningful (i.e., positive) solution of Eq. (25):

$$z'_{NB} = \frac{1}{2p_2}\left[-p_1 + (p_1^2 - 4p_0p_2)^{\frac{1}{2}}\right] \quad (27)$$

Fig. 6 shows values of z_{NB} for different values of (B_0, $\mathrm{d}\beta/\mathrm{d}z$) determined using the diapir-conduit model (plain lines) and the above expression (dashed curves). The very good agreement between Eq. (27) and the full solutions of the diapir-conduit model confirms that the assumptions made in Eq. (22) are reasonably valid. Interestingly, a quick inspection of Eqs. (26) and (27) shows that z'_{NB} does not depend directly on γ^* or B_T. However, γ^* has an indirect influence on z'_{NB} since it modifies the influx Q which affects the value of Pe, according to Eq. (20).

The comparison between numerical experiments (i.e., NE1 and NE2) and semi-analytical runs (i.e., SA1 and SA2) shows that, although it is relatively simple, our semi-analytical model is able to reproduce the essential dynamical behavior of such complex system as thermochemical plumes.

4.1.3. Regime diagram

In order to extend the above comparisons to a wide parameter space we performed 131 numerical experiments in the case where $\mathrm{d}\beta/\mathrm{d}z = 0$ for which we varied systematically B_0 and B_T. Since both B_0 and B_T are related through $\Delta\rho_0 = \rho_0 \alpha \Delta T(1 - B_0)$, they are not independent of each other and therefore when running numerical experiments, it is not practical to vary one of these numbers without changing the other. For that reason, it is more convenient to rewrite B_T as $B_T = 4/(3\gamma^*(1 - B_0))$ by substituting the expression for Q given by Eq. (21) into Eq. (19). We then vary B_0 and γ^*, the viscosity ratio between the plume and the surrounding mantle, which is equivalent to varying separately B_0 and B_T. For the numerical experiments, we systematically varied B_0 and γ, the maximum viscosity contrast which enters into Eq. (3). Then, γ^* is deduced using $\gamma^* = \gamma/1.95$.

The results are shown in Fig. 7 which displays three different regimes for the thermochemical plume as a function of γ^* and B (or equivalently β). The numerical experiments are represented by symbols while gray shading indicates the results of the semi-analytical plume model. Three distinct regimes are represented: (i) the plume reaches the upper mantle (light gray and circles), (ii) the position of the plume head oscillates vertically in the lower mantle (medium gray and triangles), (iii) no plume is formed (dark gray and squares). The exact criteria for the third regime was arbitrarily defined as the plume conduit height being less than the diameter of the plume head. The hollow symbols indicate a transition from one regime to another for the numerical experiments. Uncertainties in resolving more sharply the regimes for the numerical experiments arise because (1) the plume head is not spherical; (2) viscous entrainment takes place at the top of the plume head (especially during the descending phase) where purely thermal plumes are generated that

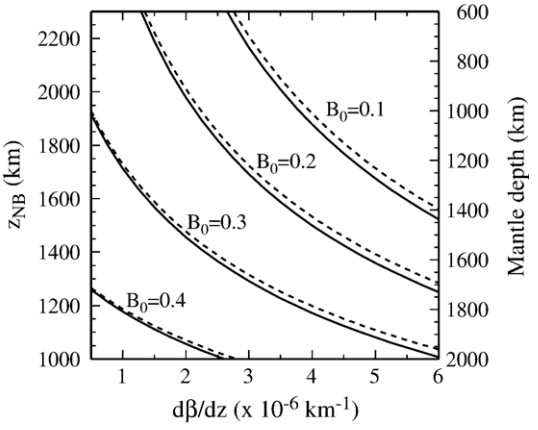

Fig. 6. Vertical location of z_{NB}, the level of neutral buoyancy of the plume head as a function of $\mathrm{d}\beta/\mathrm{d}z$ and for various values of the buoyancy number $B = B_0$ (i.e., taken at the base of the lower mantle). These calculations correspond to a plume conduit radius $r_c = 45$ km and a viscosity ratio $\gamma^* = 50$. $Pe = \frac{r_c^3 \alpha \Delta T(1-B_0) g \gamma^*}{8\eta_0 \kappa}$ is calculated using Eqs. (20) and (21). Plain line: results of the semi-analytical model. Dashed line: results using the full analytical expression of z_{NB} (i.e., Eq. (27)).

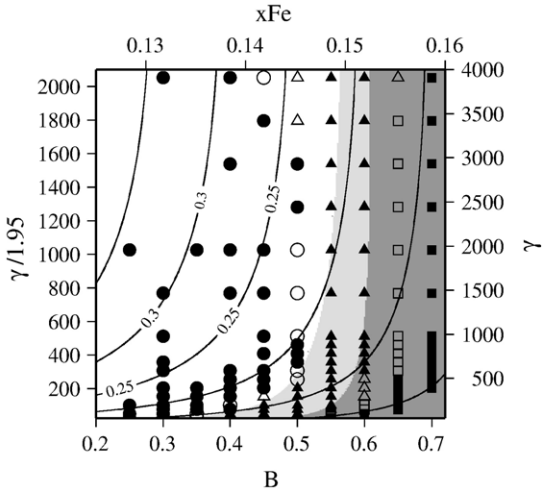

Fig. 7. Regime diagram for the case where $d\beta/dz=0$ as a function of the mean viscosity ratio $\gamma^*=\gamma/1.95$ and the buoyancy number B. The left vertical axis is the maximum viscosity contrast allowed (γ). The top horizontal axis represents the equivalent iron molar ratio xFe for the chemically denser material, assuming the same Si content for the chemically distinct material and the reference pyrolitic mantle (i.e., xSi=0.68). Shaded areas: results from the semi-analytical plume feeding model. Symbols: results from numerical experiments, with hollow symbols indicating a transition from one regime to another. Three different regimes of the thermochemical plume are mapped: (1) light gray and circles: the plume head reaches the upper mantle; (2) medium gray and triangles: oscillatory regime of the plume head in the lower mantle; (3) dark gray and squares: no plume forms. Black lines: isocontours (every 0.05 km^3/yr) of the volumetric influx Q calculated using Eq. (21). See text for further details.

tend to entrain parts of the chemically distinct material while the rest of it sinks back toward the source.

Note that for the semi-analytical calculations the plume conduit radius r_c (and consequently Q) is not the same for each case but varies with the viscosity contrast γ. Indeed, using the results of [29] one can show that the dependence of r_c with γ follows a power law:

$$r_c = a_1 + a_2\gamma^{-a_3} \quad (28)$$

where a_2 and a_3 are two positive constants that depend on various parameters such as the radius of the heating patch or the reference viscosity considered [29]. We have chosen $a_1=-33$ km, $a_2=110$ km and $a_3=0.0926$, for which Eq. (28) gives a good fit to the r_c values measured from our numerical experiments.

As clearly shown in Fig. 7 the increase of B moves the plume behavior from the regime where the plume head reaches the upper mantle to the non-plume regime, regardless the value of γ. However, γ can have a large influence on the plume's dynamical behavior, especially for relatively low γ. This is due to the fact that γ controls r_c (as shown by Eq. (28)) and Q (according to Eq. (21)). Indeed, the plot of Q in the same regime diagram (black lines), displays a comparable shape to the boundary between the different regimes of Fig. 7. This indicates that for relatively small γ (i.e., <500), an increase in γ acts the opposite way as an increase in B, by increasing the input flux Q which makes the thermochemical plume 'stronger'. However, for relatively moderate and high values of γ (i.e., >500), an increase in γ does not significantly affect the input flux Q because it is compensated by a decrease in the plume radius, according to Eq. (28), thus implying a $dQ/d\gamma\sim 0$. This results in a weak influence of γ on the dynamical behavior of the plume for large γ, as shown in Fig. 7. Therefore, the relationships between γ, r_c and Q control the shape of the boundary between the regime shown in Fig. 7.

The good agreement between numerical experiments values and semi-analytical calculations validates our diapir-conduit model for a large parameter space (B,γ).

5. Discussion

Several implications can be drawn from the numerical experiments and semi-analytical results presented above. First, the oscillatory and stagnant plume head behaviors can lead to drastically different interpretations of seismic tomography of the lower mantle. Indeed, following [5], we calculate the shear wave seismic velocity anomalies for NE1 and NE2 and SA1 and SA2 after 500 Myr. In all cases, we find broad (~1000–1400 km wide), significant (c.a. ~ −3%) slow shear wave anomalies for the plume head in the lower mantle. In all cases the shapes of the predicted seismic velocity anomalies correspond to the location of the hot and chemically distinct material (Fig. 2)

and compare well with several tomographic images of the Indo-Atlantic region [30]. However, their interpretation in terms of flow is radically different since these broad negative seismic velocity anomalies can be attributed to either: (i) to upwelling or downwelling flows, corresponding to a Fe enrichment only of the thermochemical plume (NE1 and SA1); (ii) to a vertically stagnant flow, corresponding to a Si enrichment of the thermochemical plume (NE2 and SA2). Therefore, the nature of the compositionally distinct material which dictates the dynamical behavior of thermochemical plumes has also a first order impact on the interpretation of seismic tomography of the lower mantle and emphasizes how carefully such interpretation should be done, especially in terms of the competing effects of temperature, composition and flow.

In addition, the variability of β with pressure or depth may lead to a very efficient mechanism for preserving early compositional heterogeneities, possibly inherited from the early differentiation of the Earth's mantle.

Finally, although we have essentially focused on relatively simple thermochemical plumes, we believe that the main results presented here still hold for more complex and realistic situations, such as non-axisymmetry due to plate motion at the surface or interactions between several plumes [16]. Indeed, even for more complex flows we expect that the mutual influences of mineralogy and pressure will have a first order impact on the dynamics of thermochemical plumes, as long as the feeding conduit and the plume head remain connected. However, if the plume head is separated from its conduit the heat loss by thermal diffusion will not be compensated by the supplying conduit. Therefore, one should expect that (1) a complete damping of the plume head oscillations after the plume head reaches its maximum height in the oscillatory regime (i.e., for $\mathrm{d}\beta/\mathrm{d}z=0$); (2) the stagnant plume head regime (i.e., for $\mathrm{d}\beta/\mathrm{d}z\neq 0$) would no longer exist since the necessary condition of the thermal balance $\mathrm{d}\theta_\mathrm{h}/\mathrm{d}t=0$ (e.g., see Eq. (22)) will never be met. Nevertheless, even in that case, the influence of variable compositional density contrast with pressure should have an effect on the maximum height reached by the thermochemical plume head.

6. Conclusions

On the basis of mineral physics considerations, for an assemblage of the lower mantle phases $(\mathrm{Mg,Fe})\mathrm{SiO_3}$ perovskite and (Mg,Fe)O magnesiowüstite, the compositional density contrast induced by the presence of compositional heterogeneity $\Delta\rho_\chi/\rho$ may significantly vary with pressure in the lower mantle (up to 200%), depending on the Si and Fe enrichment of the chemically distinct material.

We have thus investigated the effect of these mutual influences of mineralogy and pressure on the dynamics of axisymmetric thermochemical plumes in the lower mantle, using both numerical and, for the first time, analytical theory.

Our results show that depending on the composition, the effect of pressure can be considerable: (1) For relatively low Si enrichment, $\Delta\rho_\chi/\rho$ is fairly constant with pressure and an oscillatory behavior of the plume head is observed, similar to previous laboratory experiments [1] but without the need of a large volume of chemically distinct material. (2) For Si-enriched compositions with respect to a pyrolitic mantle, the compositional density excess increases significantly with decreasing pressure implying the presence of large volume, stagnant plume heads at a level of neutral buoyancy, which can be located at various lower mantle depths. We have provided a full analytical expression for this level of neutral buoyancy (27).

As a consequence of the revealed dynamics, these thermochemical plumes may display broad ($\sim$1200 km wide) negative seismic velocity anomalies in the lower mantle. In the case of Fe enrichment and relatively low Si enrichment of the chemically distinct material, these broad seismic velocity anomalies can be associated with upwelling or downwelling flows since the vertical locations of plume heads can oscillate with time. However, for an Si-enriched composition of the chemically distinct material, the broad seismic velocity anomalies induced by the presence of the large thermochemical plume head, are associated with vertically stagnant flows since the plume head remains at a level of neutral buoyancy.

Finally, our results show that the variability of β with lithostatic pressure may represent a very efficient mechanism to preserve primordial or recycled compositional heterogeneities for long periods, as suggested by the geochemical record and geophysical observations.

Acknowledgements

We thank Yanick Ricard for introducing us to the marker chain technique, Peter van Keken for his useful advice, Paul Tackley for providing his numerical code and an anonymous reviewer whose comments improved the manuscript. H. Samuel was sponsored by Bateman and Lavoisier fellowships. Figures were made with the Generic Mapping Tools (P. Wessel and W.H.F Smith, EOS, Trans. AGU 76 (1995) 329).

Appendix A. Calculation of compositional density contrasts

The calculation of density of a given mineralogical assemblage of $(Mg,Fe)SiO_3$ perovskite and (Mg,Fe)O magnesiowüstite is performed by proceeding as follows: We start with a given molar composition xSi, xFe. As mentioned earlier, we consider a constant value for the iron–magnesium partition coefficient between magnesiowüstite and perovskite: $K\mathrm{Fe}=3.5$. Therefore, in order to determine the iron content in perovskite $x\mathrm{Fe}^{pv}$ and in magnesiowüstite $x\mathrm{Fe}^{mw}$, we solve the following set of equations:

$$K\mathrm{Fe} = \frac{x\mathrm{Fe}^{mw}(1-x\mathrm{Fe}^{pv})}{x\mathrm{Fe}^{pv}(1-x\mathrm{Fe}^{mw})} \tag{A.1}$$

$$x\mathrm{Fe} = x\mathrm{Fe}^{mw}x\mathrm{Si} + x\mathrm{Fe}^{pv}(1-x\mathrm{Si}) \tag{A.2}$$

Then for each of the two mineralogical phases, we consider a third order finite strain formalism [33] according to which the pressure P is

$$P = \frac{3}{2}K_T\left[\left(\frac{\rho}{\rho_0}\right)^{\frac{7}{3}} - \left(\frac{\rho}{\rho_0}\right)^{\frac{5}{3}}\right]\left\{1+\frac{3}{4}(K'-4)\left[\left(\frac{\rho}{\rho_0}\right)^{\frac{2}{3}}-1\right]\right\}, \tag{A.3}$$

where ρ_0 and ρ are the room temperature densities of the mineralogical phase considered (i.e., $(Mg,Fe)SiO_3$ perovskite or (Mg,Fe)O magnesiowüstite) at room pressure and at a given pressure P, respectively, and K' is the pressure derivative of the isothermal bulk modulus K_T. These parameters are given in Table 1. We first calculate ρ_0 for each mineralogical phase, using Table 1, then we use Eq. (A.3) to calculate ρ at a given pressure P. Next we calculate the volumetric proportion of perovskite φ_{pv} and of magnesiowüstite $\varphi_{mw}=1-\varphi_{pv}$ in the assemblage, using the molar proportions of perovskite (xSi) and magnesiowüstite ($1-x$Si) and the molar volumes (i.e. the density divided by the molar mass) of each phase deduced by using Eq. (A.3). Then, the density of the whole assemblage of the two phases is calculated by doing a Voigt (volume weighted) averaging $\rho=\rho^{pv}\varphi^{pv}+\rho^{mw}(1-\varphi^{pv})$, where the superscripts pv and mw stand for $(Mg,Fe)SiO_3$ perovskite and (Mg,Fe)O magnesiowüstite, respectively. Then, by applying the approach described above while systematically varying xFe and xSi, one can obtain various density profile curves, as shown in Fig. 1. If for simplicity one neglects their curvature, these profiles can be defined to first order by β_0 (i.e., β at 125 GPa) and $d\beta/dz$.

Appendix B. Relationship between γ^* and γ

Here we determine the relationship between γ^* the viscosity ratio used for the diapir-conduit model, and γ the maximum viscosity contrast allowed in the numerical experiments. We first must consider the dimensionless temperature profile $\theta(r)$ in the plume conduit at a given height z. From our numerical experiments and previous work (e.g. [29]), $\theta(r,z)$ can be well approximated by a quadratic function:

$$\theta(r,z) = \theta_0(z)\left[1-\left(\frac{r}{r_T}\right)^2\right], \tag{B.1}$$

where $\theta_0(z)=\theta_0(r=0,z)$ and r_T is the radius for which $\theta(z)=\theta_0(z)/2$. Moreover, according to Olson et al. [29], r_c and r_T are related as follows:

$$r_c = \left(\frac{2}{\theta_0(z)\ln\gamma}\right)^{1/2} r_T \tag{B.2}$$

Using Eq. (3) one can write $\gamma^*=\exp(\bar{\theta}\ln\gamma)$, where $\bar{\theta}$ is the mean value of θ inside the plume conduit:

$$\bar{\theta} = \frac{1}{r_c}\int_0^{r_c}\theta(r)dr \tag{B.3}$$

Combining Eqs. (B.1), (B.2) and (B.3) at $z=z_0$ (and thus $\theta_0=1$) yields: $\gamma/\gamma* = \exp\left(\frac{2}{3}\right) \sim 1.95$.

Appendix C. Heat loss estimates for the diapir-conduit model

Here we determine the expressions for the conductive heat loss though the spherical diapir (q_h) and through the cylindrical conduit (q_c) which enter in the diapir-conduit model described in Section 4.

The general form of the total conductive heat flux taken at the surface of either the diapir or the conduit is:

$$q = -Sk\frac{T_{max}-T_0}{D_T}, \tag{C.1}$$

where k is the thermal conductivity, S is the area of the volume considered, T_{max} is the maximum temperature, assumed to be at the center of the volume considered (i.e., the spherical diapir or the cylindrical conduit) and T_0 is the background temperature (see Fig. 4). D_T is the

radial distance from the center of the volume considered to the radius where $T=T_0$.

Since our diapir-conduit model only deals with mean temperatures, we need to express q_h and q_c as a function of T_h and T_c, the mean temperatures of the diapir and the conduit, respectively.

C.1. Diapir

Here we use Eq. (C.1) with $S=4\pi R_h^2$ and $D_T=c_h R_h$, where c_h is a constant that has to be specified. We assume that the temperature profile inside the diapir follows a quadratic law which satisfies a Poisson's equation for steady state temperature and with constant heat generation (assumed to be provided by the advection of hot material):

$$T(R) = (T_{max}-T_0)\left[1-\left(\frac{R}{c_h R_h}\right)^2\right] + T_0, \qquad (C.2)$$

where R_h is the radius of the plume head, T_h can be obtained by taking the volume average of $T(R)$ from Eq. (C.2)

$$T_h = \frac{3}{4\pi R_h^3}\int_{R=0}^{R=R_h} 4\pi R^2 T(R)\mathrm{d}R = (T_{max}-T_0)\left(\frac{5c_h^2-3}{5c_h^2}\right) + T_0. \qquad (C.3)$$

Using Eq. (C.3), Eq. (C.1) can therefore be recast as

$$q_h = -\frac{4\pi R_h^2 k(T_h-T_0)}{R_h}\left(\frac{5c_h}{5c_h^2-3}\right). \qquad (C.4)$$

By choosing a constant value of $c_h \cong 2.3$, which is in good agreement with our numerical experiments, Eq. (C.4) simplifies to:

$$q_h \cong -2\pi R_h k(T_h-T_0). \qquad (C.5)$$

C.2. Conduit

We follow the same procedure as the one described in Section C.1. Here we use Eq. (C.1) with $S=2\pi r_c$, and $D_T=c_c r_c$, where c_c is a constant. This yields the following expression for q_c:

$$q_c = -\frac{2\pi r_c k(T_c-T_0)}{r_c}\left(\frac{2}{2c_c^2-1}\right). \qquad (C.6)$$

Since the use of Eq. (B.2) to estimate c_c, would lead to a temperature dependent c_c, we choose instead, by simplicity, a mean value of $c_c \cong 1.2$ which is close to the results of our numerical experiments. Eq. (C.6) therefore simplifies to:

$$q_c \cong -\pi k(T_c-T_0). \qquad (C.7)$$

Note that expressions (C.4) and (C.6) both include factors which depend on the geometry considered. This implies that if one wants to compare the results of the diapir–conduit model with experiments in cylindrical geometry instead of the 2D cartesian geometry, the geometric factors which enter into expressions (C.4) and (C.6) should be modified accordingly.

References

[1] A. Davaille, Simultaneous generation of hotspots and superswells by convection in a heterogeneous planetary mantle, Nature 402 (1999) 756–760.
[2] W.F. McDonough, S. Sun, The composition of the Earth, Chem. Geol. 120 (1995) 223–253.
[3] M. Javoy, The integral enstatite chondrite model of the Earth, Geophys. Res. Lett. 22 (1995) 2219–2222.
[4] A.E. Ringwood, The chemical composition and origin of the Earth, in: P.M. Hurley (Ed.), Advances in Earth Sciences, McGraw-Hill, Cambridge, 1966, pp. 287–356.
[5] H. Samuel, C.G. Farnetani, D. Andrault, Heterogeneous lowermost mantle: compositional constraints and seismological observables, in: J. Bass, R.D. van der Hilst, J. Matas, J. Tampert (Eds.), Structure Composition and Evolution of the Earth's Mantle, American Geophysical Union, Washington, DC, 2005.
[6] U.R. Christensen, A.W. Hofmann, Segregation of subducted oceanic crust in the convecting mantle, J. Geophys. Res. 99 (1994) 19,867–19,884.
[7] N. Coltice, Y. Ricard, Geochemical observations and one layer mantle convection, Earth Planet. Sci. Lett. 174 (1999) 125–137.
[8] E. Knittle, R. Jeanloz, Simulating the core–mantle boundary — an experimental study of high pressure reactions between silicates and liquid iron, Geophys. Res. Lett. 16 (1989) 609–612.
[9] A.E. Ringwood, Origin of the Earth and Moon, Springer-Verlag, New York, 1979.
[10] E. Ohtani, The primordial terrestrial magma ocean and its implication for the stratification of the mantle, Phys. Earth Planet. Inter. 38 (1985) 70–80.
[11] L.H. Kellogg, B.H. Hager, R.D. van der Hilst, Compositional stratification in the deep mantle, Science 283 (1999) 1,881–1,884.
[12] P.J. Tackley, Three-dimensional simulations of mantle convection with a thermo-chemical CMB boundary layer: D"? in: M. Gurnis, M.E. Wysession, E. Knittle, B.A. Buffett (Eds.), The Core–Mantle Boundary Region, AGU Geophys. Monogr., vol. 28, 1998, pp. 231–253.
[13] C.G. Farnetani, H. Samuel, Lagrangian structures and stirring in the Earth's mantle, Earth Planet. Sci. Lett. 206 (2003) 335–348.
[14] H. Samuel, C.G. Farnetani, Thermochemical convection and helium concentrations in mantle plumes, Earth Planet. Sci. Lett. 207 (2003) 39–56.
[15] M. Jellinek, M. Manga, The influence of a chemical boundary layer on the fixity, spacing and lifetime of mantle plumes, Nature 418 (2002) 760–763.

[16] C.G. Farnetani, H. Samuel, Beyond the thermal plume paradigm, Geophys. Res. Lett. 32 (7) (2005) L07311, doi:10.1029/2005GL022360.
[17] B. Romanowicz, Y. Gung, Superplume from the core–mantle boundary to the lithosphere: implications for heat flux, Science 296 (2002) 513–516.
[18] S.-C. Lin, P.E. van Keken, Multiple volcanic episodes of flood basalts caused by thermochemical mantle plumes, Nature 436 (2005) 250–252.
[19] F. Guyot, M. Madon, J. Peyronneau, J.-P. Poirier, X-ray microanalysis of high-pressure/high-temperature phases synthesized from natural olivine in a diamond-anvil cell, Earth Planet. Sci. Lett. 90 (1988) 52–64.
[20] N.M. Ribe, The dymanics of plume–ridge interaction 2. Off-ridge plumes, J. Geophys. Res. 96 (1996) 16195–16204.
[21] P.J. Tackley, Effects of strongly variable viscosity on three-dimensional compressible convection in planetary mantles, J. Geophys. Res. 101 (1996) 3311–3332.
[22] P.E. van Keken, S.D. King, H. Schmeling, U.R. Christensen, D. Neumeister, M.-P. Doin, A comparison of methods for the modeling of thermochemical convection, J. Geophys. Res. 102 (1997) 22,477–22,495.
[23] P.J. Tackley, S.D. King, Testing the tracer ratio method for modeling active compositional fields in mantle convection simulations, Geochem. Geophys. Geosyst. 4 (4) (2003), doi:10.1029/2001GC000214.
[24] S. Zhong, B.H. Hager, Entraiment of a dense layer by thermal plumes, Geophys. J. Int. 154 (2003) 666–676.
[25] J.A. Whitehead, D.S. Luther, Dynamic of laboratory diapir and plume models, J. Geophys. Res. 80 (1975) 705–717.
[26] P. Olson, Hot spots, swells and mantle plumes, in: M.P. Ryan (Ed.), Magma Transport and Storage, Whiley, Chichester, 1990, pp. 33–51.
[27] G.K. Batchelor, An Introduction to Fluid Dynamics, Cambridge University Press, Cambridge, 1967.
[28] D. Bercovici, A. Kelly, The non-linear initiation of diapirs and plume heads, Phys. Earth Planet. Inter. 101 (1997) 119–130.
[29] P. Olson, G. Schubert, C. Anderson, Structure of axisymmetric mantle plumes, J. Geophys. Res. 98 (1993) 6829–6844.
[30] A. Davaille, E. Stultzmann, G. Silveira, J. Besse, V. Courtillot, Convective patterns under the Indo-Atlantic "box", Earth Planet. Sci. Lett. 239 (2005) 233–252.
[31] M. Matsui, Molecular dynamics simulation of $MgSiO_3$ perovskite and the 660-km seismic discontinuity, Phys. Earth Planet. Inter. 121 (2000) 77–84.
[32] Y. Wang, D.J. Weidner, $(\partial\mu/\partial T)_P$ of the lower mantle, Pure Appl. Geophys. 146 (1996) 533–549.
[33] F. Birch, Elasticity and constitution of the Earth's interior, J. Geophys. Res. 57 (1952) 227–286.